

Wetting and Coalescence of Drops of Self-Healing Agents on Electrospun Nanofiber Mats

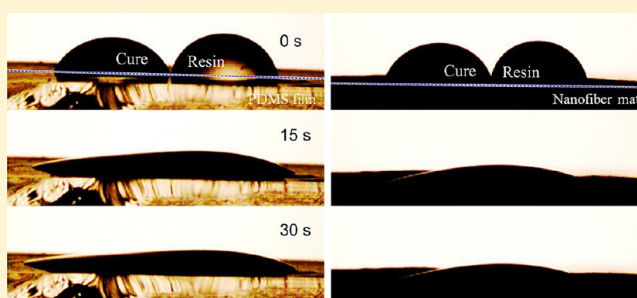
Seongpil An,^{†,‡,||} Yong Il Kim,^{†,||} Min Wook Lee,[§] Alexander L. Yarin,^{*,†,‡,||} and Sam S. Yoon^{*,†,||}

[†]School of Mechanical Engineering, Korea University, Seoul 02841, Republic of Korea

[‡]Department of Mechanical and Industrial Engineering, University of Illinois at Chicago, 842 W. Taylor Street, Chicago, Illinois 60607-7022, United States

[§]Multifunctional Structural Composite Research Center, Institute of Advanced Composites Materials, Korea Institute of Science and Technology, Chudong-ro 92, Bondong-eup, Wanju-gun, Jeollabuk-do 55324, Republic of Korea

ABSTRACT: Here we study experimentally the behavior of liquid healing agents released in vascular core–shell nanofiber mats used in self-healing engineered materials. It is shown that wettability-driven spreading of liquid drops is accompanied by the imbibition into the nanofiber matrix, and its laws deviate from those known for spreading on an intact surface. We also explore coalescence of the released drops on nanofiber mats, in particular, coalescence of drops of resin monomer and cure important for self-healing. The coalescence process is also affected by the imbibition into the pores of an underlying nanofiber mat. A theoretical model is developed to account for the imbibition effect on drop coalescence.



1. INTRODUCTION

Self-healing materials hold great promise for engineering, since concerns related to durability, reliability, and sustainability of engineered products emerged as a major issue in various industries and military applications.^{1–18} Among the numerous approaches proposed to introduce self-healing properties into engineered materials, an embedded vascular system with encased self-healing agents attracted significant attention. Hollow tube-based self-healing materials were reported first in the 1990s.¹⁹ The core–shell vascular system containing self-healing agents is advantageous in many respects, such as high healing agent content, outstanding healing agent distribution, controllable transparency, and so on.^{20–25} Electrospun core–shell nanofibers (NFs) were first introduced as a vascular system containing self-healing agents in 2010.²⁶ The present group employed both coelectrospinning and solution blowing to form NFs containing self-healing agents.^{24,25,27–33}

In the above-mentioned studies related to core–shell NFs containing self-healing agents, optimum core–shell NF fabrication conditions were explored, and the recovery of mechanical and adhesive properties, suppression of microcrack growth and propagation, and the anticorrosive performance were studied in detail. First steps were also done to study in detail the internal mechanisms of self-healing on the microscopic level starting from the release of a liquid healing agent from a damaged channel.^{31,33} Nevertheless, multiple additional details of the self-healing process on the physical level are still challenging. Accordingly, here we explore the behavior of liquid healing agents released in vascular NF mats.

2. EXPERIMENTAL SECTION

2.1. Materials. Self-healing agents, dimethylvinyl-terminated dimethylsiloxane (resin) and methylhydrogen dimethylsiloxane (cure),^{24,25,27–32} were purchased from i-Nexus (Republic of Korea). Electrospinning materials, polyacrylonitrile (PAN, $M_w = 150$ kDa) and solvent *N,N*-dimethylformamide (DMF, 99.8%), were purchased from Sigma-Aldrich (U.S.A.).

2.2. Experimental Setups for Nanofiber Mat Fabrication and Droplet Wetting/Coalescence. To fabricate nanofiber (NF) mats, an 8 wt % PAN solution was prepared first by dissolving PAN in DMF and magnetically stirring for 1 day at room temperature. Then, the PAN solution was supplied to a fixed syringe, which was equipped with an 18-gauge needle (Nordson EFD, U.S.A.), by using a syringe pump (Legato 101, KD Scientific) with a flow rate of $Q_{es} = 800 \mu\text{L}/\text{h}$. Simultaneously, a high DC voltage of $V_{es} = 12.5$ kV was applied to the needle by using a DC power supply (EL20P2, Glassman High Voltage). As a result, the PAN solution jet which was issued from the needle exit was electrospun, underwent the bending instability in flight, thinned, solvent evaporated from it, and a dry NF mat was formed onto a collector counter-electrode. The mat thicknesses were in the 33–135 μm range, which is typical for electrospun mats. The thickness variation aimed at the elucidation of the enhanced mat imbibition on drop spreading and coalescence. The collector was a drum rotating with the angular speed of 200 rpm. The distance between the needle and the collector was 12 cm. A drum collector was used to fabricate large-area NF mats. Each fabricated NF mat size was 1130 cm^2 . This size was large enough to conduct all the experiments using samples cut from the same batch. The fabricated NF mats had different thicknesses (h_{NF}), namely, $h_{NF} = 33 \pm 1.4$, 68 ± 1.5 , and $135 \pm 1.6 \mu\text{m}$, which was achieved by varying the electrospinning

Received: August 22, 2017

Revised: September 10, 2017

Published: September 11, 2017

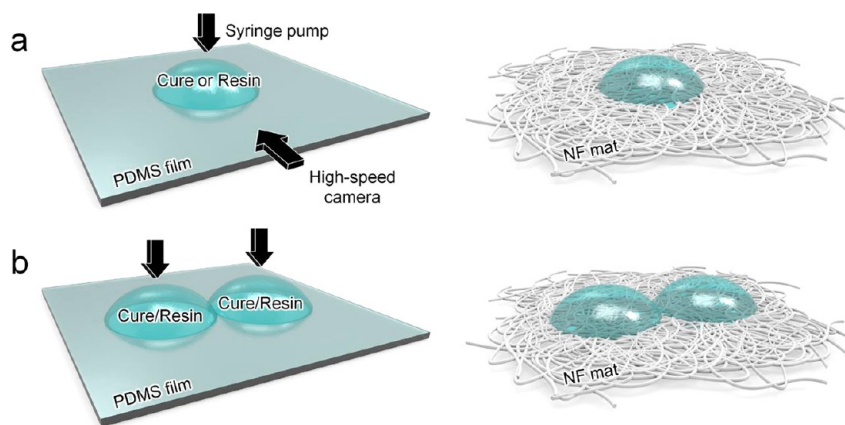


Figure 1. Schematic of (a) the wetting and (b) the coalescence experiments with two droplets, either on PDMS film (left) or NF mat (right).

time (t_{es}). Each thickness value was an averaged value, which was obtained by measuring thickness at 10 different locations of a folded-mat and then accounting for the number of folds. The area densities for the mat thicknesses $h_{NF} = 33, 68,$ and $135 \mu\text{m}$ were $0.023, 0.047,$ and 0.069 g/cm^2 , respectively. These NF mats were used as one of the substrates in the droplet coalescence experiments. A PDMS film to be used as another substrate in the droplet coalescence experiments was formed by mixing the resin and the cure solutions with the volume ratio of 10:1 and drying for 48 h at room temperature. Figure 1 depicts a schematic of the experimental process of wetting and coalescence of droplets of self-healing agents. In the wetting experiment, either a cure or a resin droplet was dripped from a syringe attached to a syringe pump (Legato 101, KD Scientific) with a flow rate of $Q_w = 3 \mu\text{L}/\text{min}$. The droplets were issued from a 23-gauge needle (Nordsion EFD, U.S.A.) attached to the syringe. The distance between the needle and a substrate (PDMS film or NF mats) was 6 mm.

In the coalescence experiments, cure and resin droplets were dripped at different flow rates of $Q_c = 200 \mu\text{L}/\text{h}$ and $800 \mu\text{L}/\text{h}$, respectively, to match the dripping time. The distance between the needle and the substrates was 7 mm. Note that all the wetting and coalescence experiments were carried out on stainless steel substrates to make the samples flat and avoid significant wrinkles.

2.3. Characterization. A high-speed camera (Vision Research, U.S.A.), which was vertically aligned over substrate (PDMS film or NF mat) at same height, was used to capture spreading droplets. An electronic caliper (CD-15 CPX, Mitutoyo, Japan) was used to measure the mat thickness. I'MEASURE software (INGPLUS, Republic of Korea) was used to measure the radius (a), the height (h), and the bridge height (H_b). Viscosity (μ) and surface tension (σ) values of self-healing agents were measured by using a rotational rheometer (DHR-1, TA Instruments, U.S.A.) and a contact angle analyzer (Phoenix 300 Touch, SEO), which is based on the pendant drop method, respectively.^{34–36} Both devices were examined by the Korea Polymer Testing & Research Institute (KOPTRI, Seoul, Republic of Korea). Sample temperature during the measurements was maintained at 25°C . The surface roughness was measured by using a noncontacting optical profiler (NT-1100, Veeco, U.S.A.) and then the roughness value (R_q) was calculated by the root-mean-square deviation (RMSD) method.

3. RESULTS AND DISCUSSION

3.1. Wetting of Self-Healing Agents on Porous Electrospun Nanofibers. The observed impact velocity (V_0) of droplets onto the substrate (PDMS film and NF mats) was relatively low, $V_0 \approx 0.2 \text{ m/s}$, due to the small nozzle-to-substrate distance (cf. Section 2.2). At such low impact velocity, there was no splashing or bouncing. It is known that the compressibility effect is negligible for the impact velocity range of $1 < V_0 < 30 \text{ m/s}$.³⁷

Figure 2 show the experimental results for the cure and resin droplet spreading in time, t , and depending on the NF mat thickness, h_{NF} . Note that t ranges for the cure and resin droplets were 0–3 and 0–300 s, respectively. In the cases of the PDMS film and the NF mat with the $h_{NF} = 33 \mu\text{m}$, the radius (a) of the spreading droplet gradually increased as t increased, whereas the height (h) of the spreading droplet decreased (Figure 2a,b,e,f). In contrast to these cases, a different radius trend was observed at the NF mats with the higher thicknesses, $h_{NF} = 68$ and $135 \mu\text{m}$. The radius a of the cure droplet on the NF mats with $h_{NF} = 68$ and $135 \mu\text{m}$ revealed a different behavior in comparison with the case of the NF mat with $h_{NF} = 33 \mu\text{m}$. Namely, the radius a initially increased but then started to decrease after the moments $t = 1$ and 0.5 s , respectively, on these thicker NF mats (Figure 2c,d).

These different trends observed in droplet spreading on the thicker NF mats with $h_{NF} = 68$ and $135 \mu\text{m}$ in comparison with the thinner NF mat with $h_{NF} = 33 \mu\text{m}$ and on the PDMS film were attributed to the enhanced effect of porosity of the thicker NF mats. The overall pore volume in the thicker NF mats was quite significant, and liquid was gradually absorbed into them. The mats were highly wettable by the resin and cure, as illustrated in Figure 3. The surface roughness of the NF mats was also affected by the electrospinning time, t_{es} (which also affects the thickness h_{NF}), as shown in Table 1, where the surface roughness, R_q , increased from 3.04 to $3.53 \mu\text{m}$ as the h_{NF} increased. The contact surface area between the droplet and the NF mat is increased as the R_q increased, which facilitated the absorption of liquid into the NF mats.

For a resin droplet, its footprint radius a on the mat with $h_{NF} = 68 \mu\text{m}$ exhibited a slight increase (Figure 2g). This also was the case for the resin droplet on the mat with $h_{NF} = 135 \mu\text{m}$, albeit after that in both these cases the increase of a in t was ceased, and in the latter case, it essentially decreased after the moment $t = 100 \text{ s}$ (Figure 2h). Note also that the capillary numbers (Ca) in all cases are similar, namely, $Ca \approx 8 \times 10^{-3}$. Such spreading regimes are generally considered being viscosity-dominated rather than capillarity-dominated.³⁸ In addition, it should be emphasized that the magnitude of the rate of variation of h was increased as h_{NF} increased (cf. Figure 2).

3.2. Coalescence of Droplets of Self-Healing Agents on Porous Electrospun Nanofibers. Figures 4–6 show the side-view images of two coalescing droplets on the PDMS film and the NF mat with $h_{NF} = 68 \mu\text{m}$. Figures 4–6 correspond to the cure–cure, the resin–resin, and the cure–resin coalescing droplets, respectively. In distinction from the wetting experiments

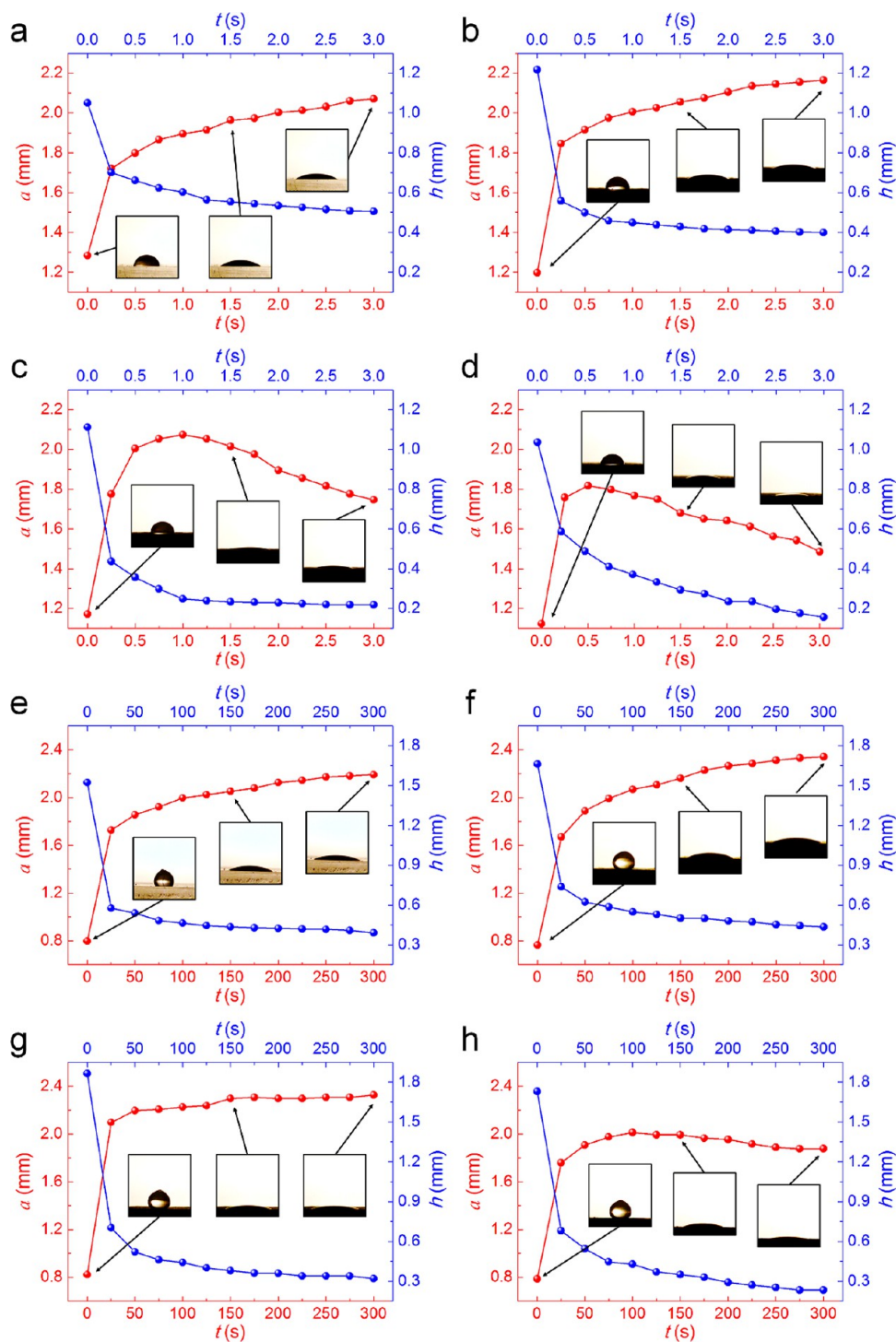


Figure 2. Droplet radius a as a function of time t for (a, c, e, and g) the cure and (b, d, f, and h) the resin droplets spreading on (a and e) the PDMS film, (b and f) the NF mat with $h_{\text{NF}} = 33 \mu\text{m}$, (c and g) the NF mat with $h_{\text{NF}} = 68 \mu\text{m}$, and (d and h) the NF mat with $h_{\text{NF}} = 135 \mu\text{m}$. Insets are the high-speed camera images of the spreading droplets.

discussed in Section 3.1, the time ranges for the cases where resin was involved (the resin–resin and the resin–cure cases shown in Figures 5 and 6, respectively) were set to 30 s sufficient for the coalescence process to be completed.

Figure 4 shows how two cure droplets coalesce on different substrates. In the case of the PDMS film (Figure 4a), the bridge height of the two merging droplets, H_b , increased until $t = 2$ s and then became constant after $t = 2$ s. The bridge height H_1 in the case of coalescence on the NF mat with the thickness of $h_{\text{NF}} = 68$

μm also increased until $t = 1$ s (Figure 4b), but after that started to decrease. This phenomenon was attributed to the imbibition of liquid into the NF mat as revealed by the wetting experiments (cf. Section 3.1).

Figure 5a,b illustrate how two resin droplets coalesce on the PDMS film and the NF mat with the thickness of $h_{\text{NF}} = 68 \mu\text{m}$, respectively. Similarly to the merging of two cure droplets on the PDMS film (cf. Figure 4a), the bridge height H_b increased up to $t = 7.5$ s (which snapshot is not shown in Figure 5a). After that, H_b

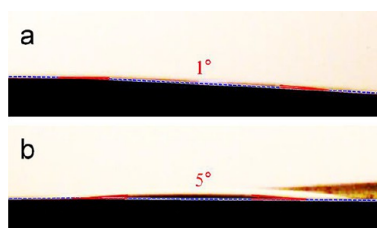


Figure 3. Side-view images which show the static contact angles of (a) the cure and (b) the resin on an intact flat PAN film.

Table 1. Surface Roughness Values of NF Mats

	NF mat thickness		
	33 μm	68 μm	135 μm
R_q (μm)	3.04	3.13	3.53

gradually decreased. In the case of the NF mat with $h_{\text{NF}} = 68 \mu\text{m}$ (Figure 5b), H_b also increased up to $t = 7.5 \text{ s}$ and decreased after $t = 7.5 \text{ s}$. The comparison of Figure 5a,b reveals not too much difference between the two resin droplets coalescence on the PDMS film and the NF mat with the thickness of $h_{\text{NF}} = 68 \mu\text{m}$.

Figure 6 shows the coalescence of different droplets on different substrates, where the droplet on the left is the cure, and the one on the right is the resin. Note that both droplets in each figure had initially equal size. In Figure 6a, the bridge height H_b on the PDMS film increased until $t = 1 \text{ s}$ (this snapshot is not shown in the figure), and then gradually decreased. In Figure 6b, the bridge H_b on the NF mat with $h_{\text{NF}} = 68 \mu\text{m}$ increased until $t = 0.3 \text{ s}$ (this snapshot is not shown in the figure), and then also

decreased. In spite of the presence of resin droplet in this pair, here in distinction from Figure 5, a significant decrease in the bridge height H_b in the case of the NF mat was clearly seen compared to the case of the PDMS film (Figure 6a). This is attributed to the lowered overall viscosity due to mixture of the resin with the cure. Therefore, when self-healing agents had been released due to microcracks from a complex mutually entangled core-shell NFs, the relatively fast polymerization reaction between the cure and resin was mainly attributed to the fast imbibition of the cure into the surrounding matrix.^{24,25,27–32} It should be emphasized that compressibility of electrospun nanofiber mats under the drop weight or the impact impulse, as well as local redistribution of filament links under the pulling action of drop liquid, are negligibly small even in the case of drop impacts with velocities up to 3.5 m/s.³⁹ This stems from the fact that electrospun NF mats are thoroughly entangled on the micron scale, which is 2 to 3 orders of magnitude smaller than the drop size. Accordingly, these effects are even more immaterial in the present case of soft deposition and slow motion of drops on electrospun NF mats.

4. THEORETICAL AND COMPARISON WITH THE EXPERIMENTAL RESULTS

4.1. Radius Changes During Wetting. The Hoffman–Voinov–Tanner law describes viscosity-dominated wettability-driven spreading of droplets on a sufficiently wettable intact substrate with negligibly small static contact angles.³³ The radius of the droplet footprint a is given as

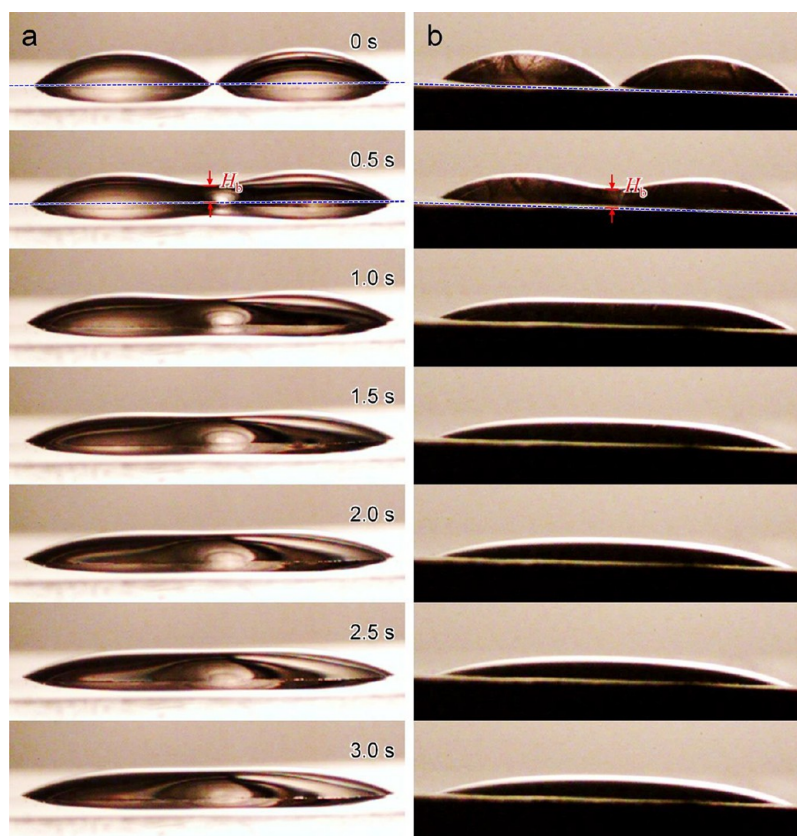


Figure 4. Side-view images of the coalescing cure–cure droplets at different time moments on two substrates: (a) the PDMS film and (b) the NF mat with $h_{\text{NF}} = 68 \mu\text{m}$.

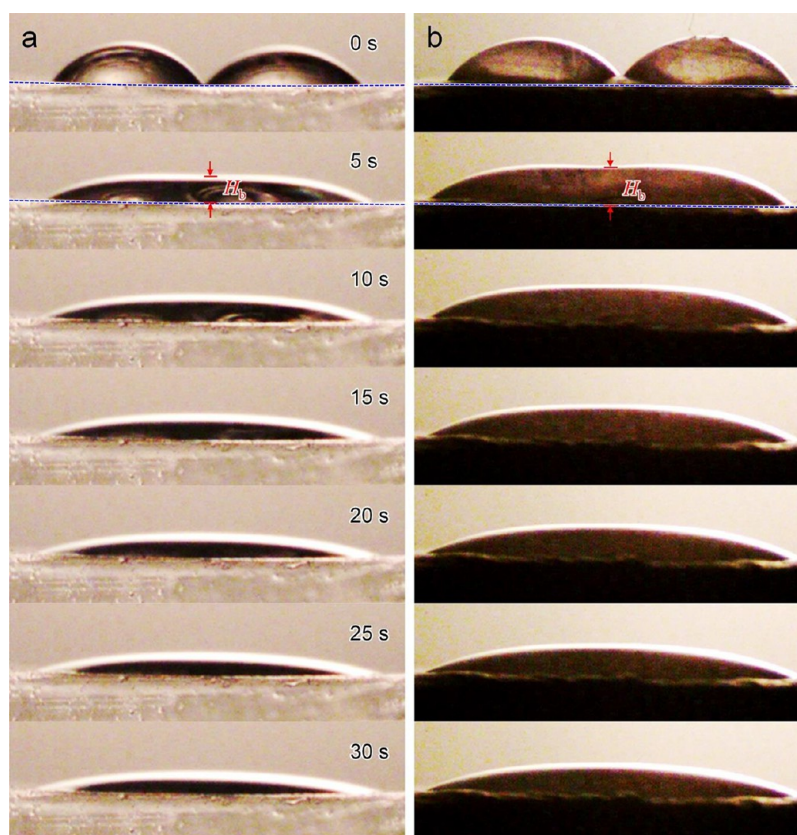


Figure 5. Side-view images of the coalescing resin–resin droplets at different time moments on two substrates: (a) the PDMS film and (b) the NF mat with $h_{\text{NF}} = 68 \mu\text{m}$.

$$a = \left\{ 0.107 \frac{\sigma}{\mu} \left(\frac{4V}{\pi} \right)^3 t \right\}^{1/10} \propto t^{1/10} \quad (1)$$

where μ and σ are the viscosity and surface tension of the liquid in the droplet, respectively; $V = 4\pi a_0^3/3$ is the droplet volume, with a_0 being the volume-equivalent droplet radius; t is the time of spreading.

The experimental results (cf. Figure 2) are compared with the theoretical predictions of eq 1. In Figure 7, the log–log scale experimental and theoretical results are presented by solid and short dashed lines, respectively. Figure 7a,b show the case of the cure and resin droplets on PDMS film. Note that the Hoffman–Voinov–Tanner law implies a perfectly wettable substrate, whereas PDMS is almost a perfectly wettable substrate for the self-healing agents (the static contact angles are $9\text{--}11^\circ$ for resin and $4\text{--}5^\circ$ for cure).³³ It should be emphasized that eq 1 is a remote asymptotics, and its comparison with the experimental data corresponding to a definite initial condition, as usual, could reveal only a scaling rather than an overlap of the two lines (thus, the gap shown by arrows in Figure 7a,b), which could result in a slight discrepancy between the theory and the experiment. It should be emphasized that the slopes of the experimental and theoretical dependences $a(t)$ in Figure 7a,b are sufficiently close.

Figure 7c–h show the comparison of the experimental results for cure droplets on NF mats of different thickness, h_{NF} , with the predictions of eq 1. Similarly to the PDMS film case (cf. Figure 7a), the experimental results at the early time agree fairly well with the theoretical results obtained from eq 1 (marked by sky-blue circles in Figure 7c,e,g). Even better, the perfect wettability of PAN by cure, with the static contact angle of about 1° as

revealed in Figure 3a, brought the predictions closer to the data, since it facilitated a rapid spreading corresponding to the remote asymptotics. However, significant deviations (marked by green circles in Figure 7c,e,g) of the data on NF mats from the predictions of eq 1 were observed after $t = 1$ s for the mat thicknesses $h_{\text{NF}} = 33$ and $68 \mu\text{m}$ (Figure 7c,e), and after $t = 0.5$ s for the mat thickness of $h_{\text{NF}} = 135 \mu\text{m}$ (Figure 7g). In particular, this trend was intensified as both time t and thickness h_{NF} increased. Over time, it seems that the cure was more imbibed into the NF mat bulk. On the other hand, the hydrodynamic time, $\tau_{\text{H}} \sim \mu/\sigma$, which controls capillarity-driven flows of highly viscous fluid (the mat imbibition in the present case),⁴⁰ is relatively low for the cure, which facilitates its imbibition.

In the case of resin droplets on NF mats, eq 1 seemingly deviated from the data even at the earlier times t (Figure 7d,f,h), which is attributed not only to the higher viscosity of resin compared to cure (cf. Table 2) but also to the only partial wettability of PAN by the resin (Figure 3b), with the static contact angle being about 5° . At a later time, there is a growing disparity between the data and the predictions of eq 1 pointing at the resin imbibition into NF mats unaccounted for by eq 1 (marked by green circles in Figure 7d,f,h).

4.2. Coalescence of Droplets. Wettability-driven suction of liquid into porous medium can be described using the following diffusion-like equation^{41,42}

$$\frac{\partial u}{\partial t} = \alpha_m \frac{\partial^2 u}{\partial x^2} \quad (2)$$

where u is the dimensionless moisture content, x represents the horizontal coordinate with its origin at the droplet center, t is time, and α_m is the moisture transfer coefficient.

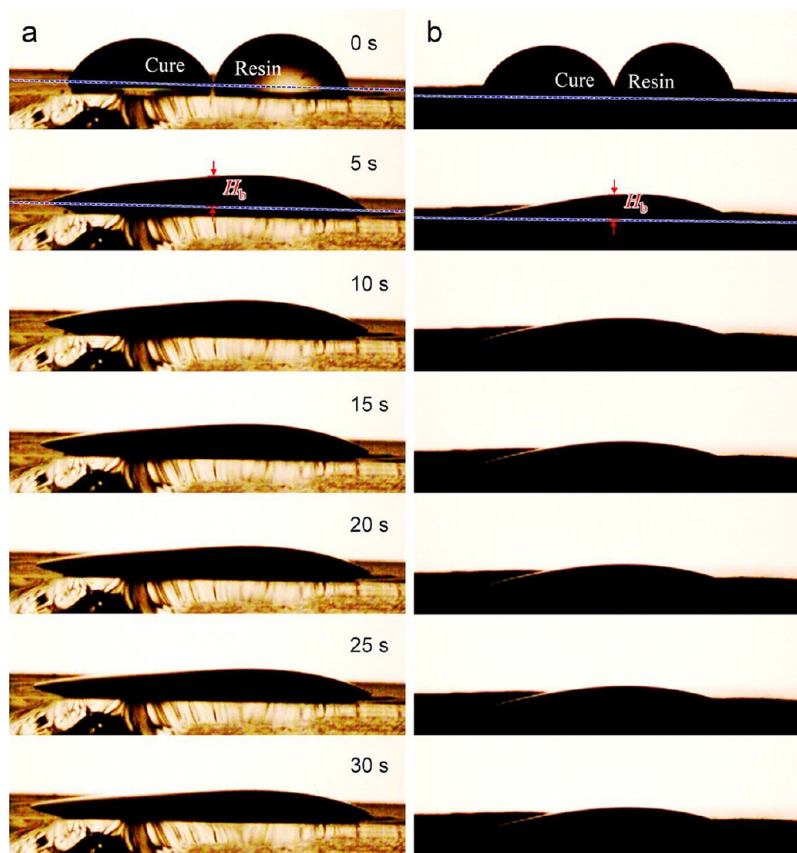


Figure 6. Side-view images of the coalescing cure–resin droplets (left–right, respectively) at different time moments on two substrates: (a) the PDMS film and (b) the NF mat with $h_{\text{NF}} = 68 \mu\text{m}$.

The solution of eq 2 is subjected to the following initial and boundary conditions

$$t = 0: u = f(x) \quad (3)$$

$$t > 0: x = \pm\infty, u = 0 \quad (4)$$

where $f(x)$ corresponds to the initial moisture distribution on the surface.

The moisture transfer coefficient is associated with liquid transport in pores driven by wettability.^{41,42} The velocity V_{LW} of the wettability-driven impregnation of pores can be evaluated using the Lucas–Washburn equation,^{43–46} $V_{\text{LW}} \sim \sigma d / (8\mu H)$, where perfect wettability is assumed. Also, d denotes a characteristic cross-sectional pore diameter, σ denotes the surface tension, μ denotes the viscosity, and H denotes a characteristic pore length. On the other hand, V_{LW} can be expressed through the moisture transfer coefficient as $V_{\text{LW}} \sim \alpha_m / (4H)$. Accordingly, $\alpha_m \sim d$. Permeability of porous media $k \sim d^2$, whereas the Kozeny–Carman equation⁴⁷ relates permeability with porosity ε as $k \sim \varepsilon^3 / (1 - \varepsilon)^2$. Then, $d \sim \varepsilon^{3/2} / (1 - \varepsilon)$, and thus $\alpha_m \sim \varepsilon^{3/2} / (1 - \varepsilon)$. Namely, as porosity increases, the moisture transfer coefficient increases as well. This dependence of the moisture transfer coefficient on porosity reveals the dependence of all the subsequent results on porosity.

The solution of the problem (eqs 2–4) is found as⁴⁸

$$u(x, t) = \frac{1}{2\sqrt{\pi}} \int_{-\infty}^{\infty} \frac{1}{\sqrt{\alpha_m t}} \exp[-(x - \xi)^2 / (4\alpha_m t)] f(\xi) d\xi \quad (5)$$

where ξ is the dummy variable.

Assume that two initial wet spots corresponding to droplets in this model are fully wet, i.e. $u = 1$ at $t = 0$ at the following two symmetrically located sections: $-l - D \leq x \leq -l$ and $l \leq x \leq l + D$. At the other locations of the surface there is no moisture at $t = 0$, i.e. $u = 0$ there. Note that D corresponds to the droplet size and $2l$ corresponds to the initial distance between the closest droplet edges. Accordingly, the function $u = f(x)$ determining the initial distribution of liquid is fully determined, and thus, the integral in eq 5 can be easily evaluated. This yields

$$u = \frac{1}{2} \{ \text{erf}[M(x - l)] - \text{erf}[M(x - l - 1)] + \text{erf}[M(x + l + 1)] - \text{erf}[M(x + l)] \} \quad (6)$$

where x and l are rendered dimensionless by D , $\text{erf}(\cdot)$ denotes the error function, and the dimensionless function of time M depends on the dimensional time t as

$$M = \frac{D}{2\sqrt{\alpha_m t}} \quad (7)$$

Note that M varies from ∞ (which corresponds to $t = 0$) to 0 (which corresponds to $t = \infty$).

The experimental observations in Figures 4–6 are recast into the dependences of the bridge height, H_b , on time t presented in Figure 8. Note that the straight dashed lines in Figure 8 illustrate the scaling trends which are suggested by the first three data points. As discussed in Section 3.2, the bridge height H_b increases at the early time moments but then begins to decrease due to the liquid surface rearrangement due to surface tension. The latter is

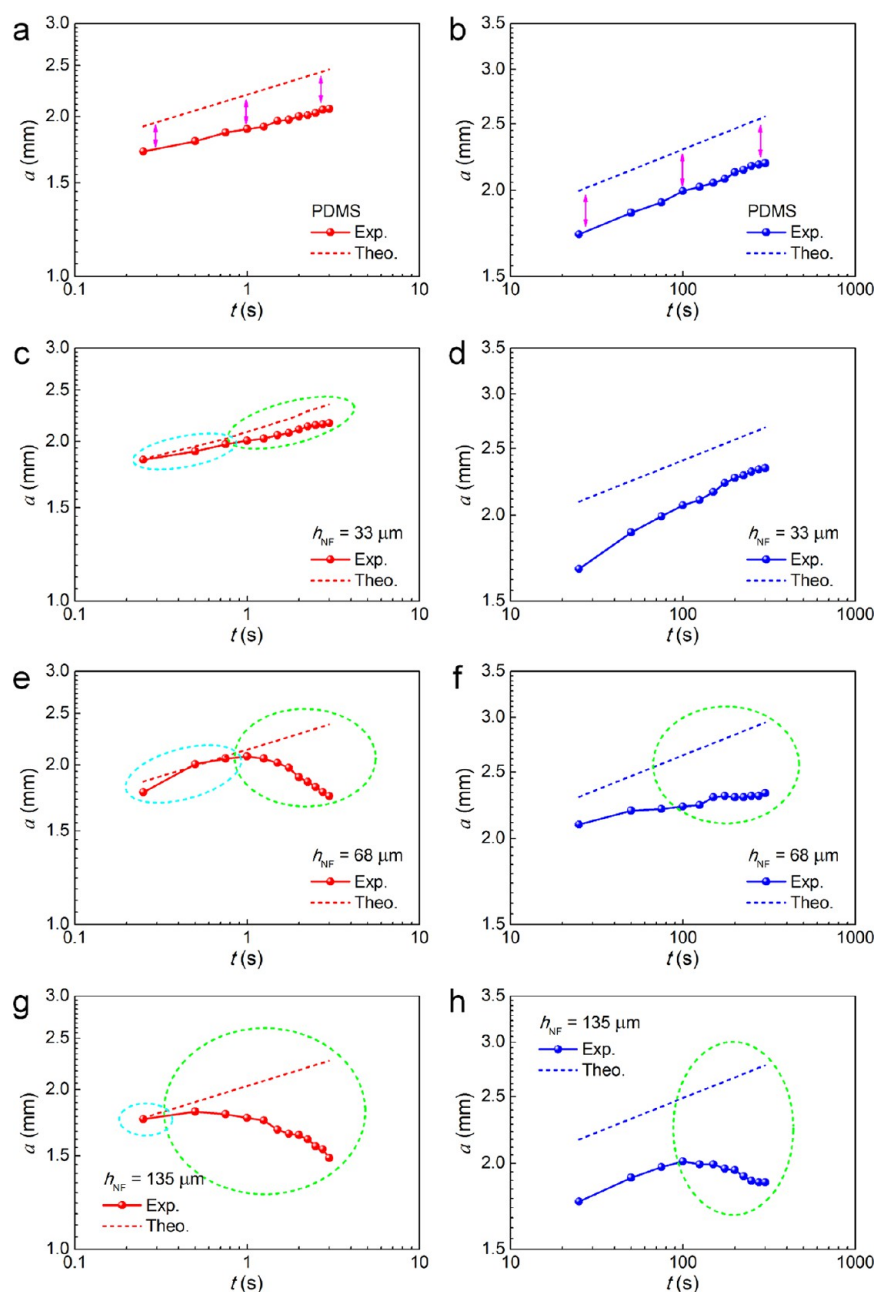


Figure 7. Comparison of the experimental and theoretical values of the radius a as a function of time t for spreading of (a, c, e, and g) cure, (b, d, f, and h) resin droplets on (a and b) the PDMS film and (c–h) the NF mats with different h_{NF} : (c and d) $h_{\text{NF}} = 33 \mu\text{m}$, (e and f) $h_{\text{NF}} = 68 \mu\text{m}$, and (g and h) $h_{\text{NF}} = 135 \mu\text{m}$.

Table 2. Viscosity and Surface Tension Values the Cure and the Resin; $\dot{\gamma}$ Denotes Shear Rate

	$\dot{\gamma}$ (s^{-1})	μ (Pa·s)	σ ($\text{mN}\cdot\text{m}^{-1}$)
cure	10	0.06	17.67
	500	0.05	
resin	10	4.97	23.94
	500	4.59	

the only physical factor at play in the case of coalescence on the intact PAN film; however, in the case of coalescence on NF mat, there is another factor—the imbibition of liquid into the pores. This latter factor was responsible for the data deviation from the dashed lines, which was much more pronounced on NF mats than on the intact PDMS film, especially in the cure–cure and

the cure–resin cases (Figure 8b,f). This effect was less pronounced in case of the resin–resin droplets on NF mat (Figure 8d) due a diminished imbibition, which stems from the relatively high viscosity of resin and a lower wettability of PAN by resin.

The data presented in Figure 8 can be compared with the predictions of the theoretical eqs 6 and 7. Figure 9a,b show the predicted moisture distributions for two coalescing cure–cure and resin–resin droplets, respectively, both on the NF mat with $h_{\text{NF}} = 68 \mu\text{m}$. These plots were obtained from eqs 6 and 7. In particular, the values of M were found using the experimentally measured geometrical parameters D and l for these two cases. The results in Figure 9 show that while the predicted values of M varied from 1 to 0 (which means that time t varied from approximately 0 to a certain large enough value), the values of the

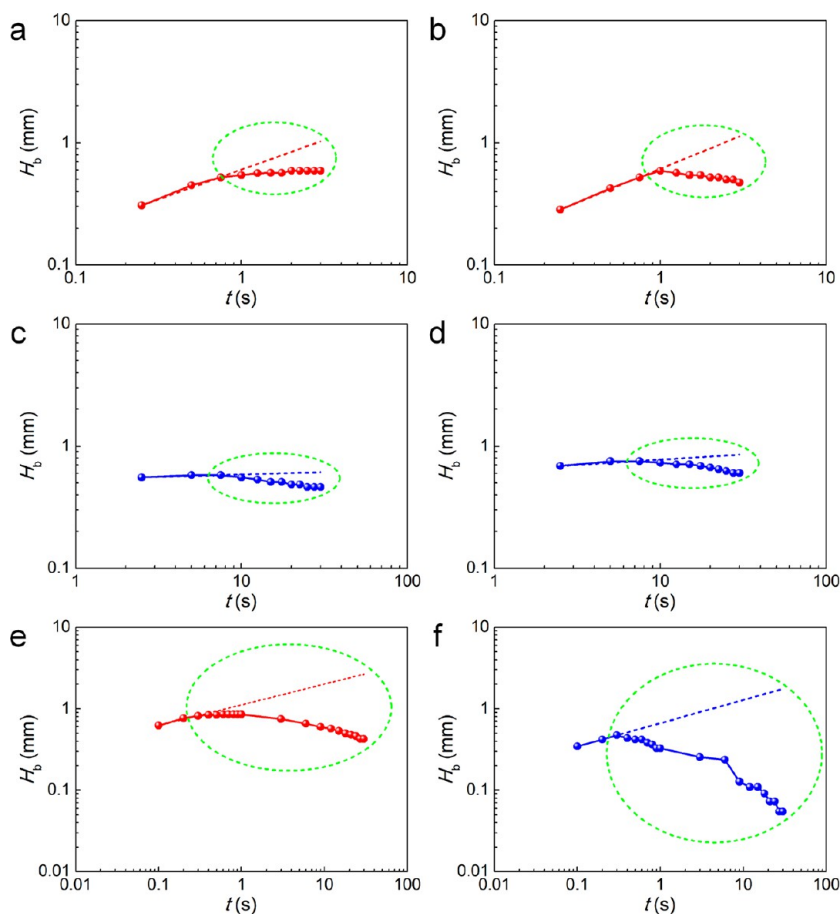


Figure 8. Bridge height H_b as a function of time t for two coalescing (a and b) cure–cure, (c and d) resin–resin, and (e and f) cure–resin droplets on (a, c, and e) an intact PDMS film and (b, d, and f) on the NF mat with $h_{\text{NF}} = 68 \mu\text{m}$. The data for the cure–cure, resin–resin, and cure–resin correspond to Figures 4, 5, and 6, respectively.

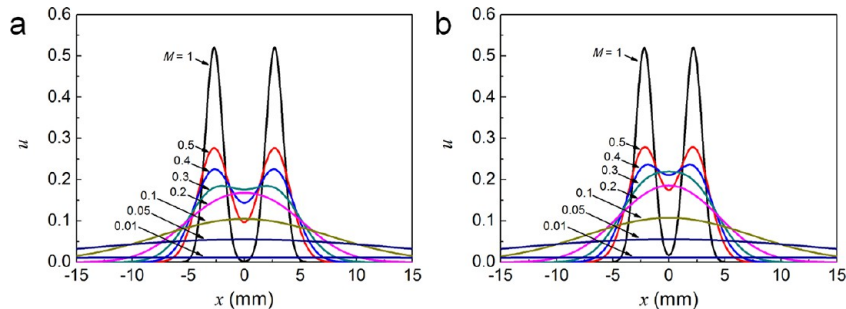


Figure 9. Moisture distributions predicted using eqs 6 and 7 for two coalescing (a) cure–cure and (b) resin–resin droplets on the NF mat with $h_{\text{NF}} = 68 \mu\text{m}$.

moisture u at the center $x = 0$ (which correspond to the bridge height H_b) in the cure–cure and resin–resin cases achieved the maximal values of $u = 0.18$ and 0.22 (for $M = 0.26$ and 0.33 , respectively). After that the values of u at $x = 0$ started to diminish and approached 0. This general trend agrees with the experimental observation, albeit a detailed fit of the theory to the experimental data is possible only when the moisture transport coefficient α_m is chosen. Accordingly, one finds the values of $\alpha_m = 1.2 \times 10^{-1}$ and $6 \times 10^{-3} \text{ cm}^2/\text{s}$ for the cure–cure and resin–resin cases on the NF mats with $h_{\text{NF}} = 68 \mu\text{m}$, respectively.

Figure 10 shows the comparison of the theory with the experimental data. In particular, Figure 10a,b illustrate the

unmatched values of the theoretically predicted u at $x = 0$ and the measured H_b , which requires factors of 3.2 and 3.5 for the cure–cure and resin–resin cases, respectively. Then, the theoretical predictions

$$\begin{aligned} H_b &= 3.2u \\ &= 1.6\{\text{erf}[M_c(x-l)] - \text{erf}[M_c(x-l-1)] \\ &\quad + \text{erf}[M_c(x+l+1)] - \text{erf}[M_c(x+l)]\} \end{aligned} \quad (8)$$

$$\begin{aligned} H_b &= 3.5u \\ &= 1.75\{\text{erf}[M_r(x-l)] - \text{erf}[M_r(x-l-1)] \\ &\quad + \text{erf}[M_r(x+l+1)] - \text{erf}[M_r(x+l)]\} \end{aligned} \quad (9)$$

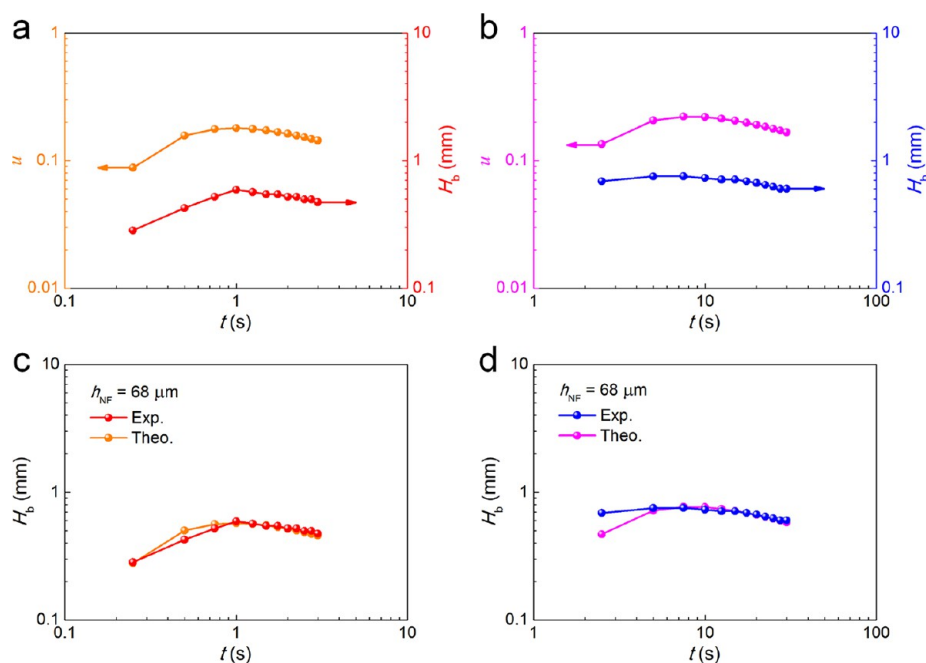


Figure 10. Theoretically predicted bridge heights (the value of u at $x = 0$) versus the experimentally measured bridge height H_b as functions of time t for two coalescing (a and c) cure–cure and (b and d) resin–resin droplets on NF mat with $h_{\text{NF}} = 68 \mu\text{m}$.

where $\alpha_m = 1.2 \times 10^{-1}$ and $6 \times 10^{-3} \text{ cm}^2/\text{s}$ for the cure–cure and resin–resin cases, respectively, describe the experimental data fairly well, as shown in Figure 10c,d.

5. CONCLUSIONS

It is shown that droplets of the healing agents, dimethylvinyl-terminated dimethylsiloxane (resin) and methylhydrogen dimethylsiloxane (cure), being released on nanofiber (NF) mats spread, touch each other and merge driven by wettability and surface tension. Moreover, polyacrylonitrile (PAN) NF mats used in this work are shown to be wettable by the resin and cure (with the static contact angles being 5° and 1° , respectively). Accordingly, coalescence of two droplets on NF mats is accompanied by significant imbibition of resin and cure into the pores. As a result, the Hoffman–Voinov–Tanner law is shown to be incapable of describing drop spreading on NF mats due to a significant effect of the imbibition, which is enhanced at the higher mat thicknesses. Moreover, a new theory was proposed to describe the experimental dependence of the bridge height between two coalescing droplets: an initial increase, and then a significant decrease enhanced by the imbibition. It was demonstrated that the theory is capable of describing the experimental data, with the moisture transport coefficient values being $\alpha_m = 1.2 \times 10^{-1}$ and $6 \times 10^{-3} \text{ cm}^2/\text{s}$ for cure and the resin, respectively. These values quantify to what extent PAN NFs are more wettable by the cure in comparison with the resin.

AUTHOR INFORMATION

Corresponding Authors

*E-mail for A.L.Y.: ayarin@uic.edu.

*E-mail for S.S.Y.: skyoona@korea.ac.kr.

ORCID

Alexander L. Yarin: 0000-0001-8032-2525

Sam S. Yoon: 0000-0002-9031-4198

Author Contributions

|| (S.A. and Y.I.K.) These authors contributed equally to this work.

Notes

The authors declare no competing financial interest.

ACKNOWLEDGMENTS

This work was supported by the International Collaboration Program funded by the Agency for Defense Development of the Republic of Korea and by the Technology Development Program to Solve Climate Changes of the National Research Foundation (NRF) funded by the Ministry of Science, ICT & Future Planning (NRF-2016M1A2A2936760), NRF-2013M3A6B1078879, and NRF-2017R1A2B4005639. This work was supported by Advanced Research Center Program (NRF-2013R1A5A1073861).

REFERENCES

- (1) Trask, R.; Williams, H.; Bond, I. Self-healing polymer composites: mimicking nature to enhance performance. *Bioinspiration Biomimetics* **2007**, *2* (1), P1.
- (2) Wu, D. Y.; Meure, S.; Solomon, D. Self-healing polymeric materials: a review of recent developments. *Prog. Polym. Sci.* **2008**, *33* (5), 479–522.
- (3) Samadzadeh, M.; Boura, S. H.; Peikari, M.; Kasirihha, S.; Ashrafi, A. A review on self-healing coatings based on micro/nanocapsules. *Prog. Org. Coat.* **2010**, *68* (3), 159–164.
- (4) Blaiszik, B.; Kramer, S.; Olugebefola, S.; Moore, J. S.; Sottos, N. R.; White, S. R. Self-healing polymers and composites. *Annu. Rev. Mater. Res.* **2010**, *40*, 179–211.
- (5) Hager, M. D.; Greil, P.; Leyens, C.; van der Zwaag, S.; Schubert, U. S. Self-healing materials. *Adv. Mater.* **2010**, *22* (47), 5424–5430.
- (6) Stankiewicz, A.; Szczygieł, I.; Szczygieł, B. Self-healing coatings in anti-corrosion applications. *J. Mater. Sci.* **2013**, *48* (23), 8041–8051.
- (7) Binder, W. H. *Self-Healing Polymers: From Principles to Applications*; John Wiley & Sons: Hoboken, NJ, 2013.

- (8) Herbst, F.; Döhler, D.; Michael, P.; Binder, W. H. Self-healing polymers via supramolecular forces. *Macromol. Rapid Commun.* **2013**, *34* (3), 203–220.
- (9) Yang, Y.; Urban, M. W. Self-healing polymeric materials. *Chem. Soc. Rev.* **2013**, *42* (17), 7446–7467.
- (10) Wei, Z.; Yang, J. H.; Zhou, J.; Xu, F.; Zrínyi, M.; Dussault, P. H.; Osada, Y.; Chen, Y. M. Self-healing gels based on constitutional dynamic chemistry and their potential applications. *Chem. Soc. Rev.* **2014**, *43* (23), 8114–8131.
- (11) Yang, Y.; Ding, X.; Urban, M. W. Chemical and physical aspects of self-healing materials. *Prog. Polym. Sci.* **2015**, *49*, 34–59.
- (12) Hillewaere, X. K.; Du Prez, F. E. Fifteen chemistries for autonomous external self-healing polymers and composites. *Prog. Polym. Sci.* **2015**, *49*, 121–153.
- (13) Wei, H.; Wang, Y.; Guo, J.; Shen, N. Z.; Jiang, D.; Zhang, X.; Yan, X.; Zhu, J.; Wang, Q.; Shao, L.; et al. Advanced micro/nanocapsules for self-healing smart anticorrosion coatings. *J. Mater. Chem. A* **2015**, *3* (2), 469–480.
- (14) Thakur, V. K.; Kessler, M. R. Self-healing polymer nanocomposite materials: A review. *Polymer* **2015**, *69*, 369–383.
- (15) Diesendruck, C. E.; Sottos, N. R.; Moore, J. S.; White, S. R. Biomimetic self-healing. *Angew. Chem., Int. Ed.* **2015**, *54* (36), 10428–10447.
- (16) Bekas, D.; Tsirka, K.; Baltzis, D.; Paipetis, A. Self-healing materials: a review of advances in materials, evaluation, characterization and monitoring techniques. *Composites, Part B* **2016**, *87*, 92–119.
- (17) Silva, A. C. M.; Moghadam, A. D.; Singh, P.; Rohatgi, P. K. Self-healing composite coatings based on in situ micro–nanoencapsulation process for corrosion protection. *J. Coat. Technol. Res.* **2017**, 1–29.
- (18) Behzadnasab, M.; Mirabedini, S.; Esfandeh, M.; Farnood, R. Evaluation of corrosion performance of a self-healing epoxy-based coating containing linseed oil-filled microcapsules via electrochemical impedance spectroscopy. *Prog. Org. Coat.* **2017**, *105*, 212–224.
- (19) Dry, C. Procedures developed for self-repair of polymer matrix composite materials. *Compos. Struct.* **1996**, *35* (3), 263–269.
- (20) Kousourakis, A.; Mouritz, A. The effect of self-healing hollow fibres on the mechanical properties of polymer composites. *Smart Mater. Struct.* **2010**, *19* (8), 085021.
- (21) Norris, C. J.; Meadway, G. J.; O’Sullivan, M. J.; Bond, I. P.; Trask, R. S. Self-healing fibre reinforced composites via a bioinspired vasculature. *Adv. Funct. Mater.* **2011**, *21* (19), 3624–3633.
- (22) Patrick, J.; Sottos, N.; White, S. Microvascular based self-healing polymeric foam. *Polymer* **2012**, *53* (19), 4231–4240.
- (23) Patrick, J. F.; Hart, K. R.; Krull, B. P.; Diesendruck, C. E.; Moore, J. S.; White, S. R.; Sottos, N. R. Continuous self-healing life cycle in vascularized structural composites. *Adv. Mater.* **2014**, *26* (25), 4302–4308.
- (24) Lee, M. W.; An, S.; Lee, C.; Liou, M.; Yarin, A. L.; Yoon, S. S. Self-healing transparent core–shell nanofiber coatings for anti-corrosive protection. *J. Mater. Chem. A* **2014**, *2* (19), 7045–7053.
- (25) An, S.; Liou, M.; Song, K. Y.; Jo, H. S.; Lee, M. W.; Al-Deyab, S. S.; Yarin, A. L.; Yoon, S. S. Highly flexible transparent self-healing composite based on electrospun core–shell nanofibers produced by coaxial electrospinning for anti-corrosion and electrical insulation. *Nanoscale* **2015**, *7* (42), 17778–17785.
- (26) Park, J. H.; Braun, P. V. Coaxial electrospinning of self-healing coatings. *Adv. Mater.* **2010**, *22* (4), 496–499.
- (27) Lee, M. W.; An, S.; Lee, C.; Liou, M.; Yarin, A. L.; Yoon, S. S. Hybrid self-healing matrix using core–shell nanofibers and capsuleless microdroplets. *ACS Appl. Mater. Interfaces* **2014**, *6* (13), 10461–10468.
- (28) Lee, M. W.; An, S.; Jo, H. S.; Yoon, S. S.; Yarin, A. L. Self-healing nanofiber-reinforced polymer composites. 1. Tensile testing and recovery of mechanical properties. *ACS Appl. Mater. Interfaces* **2015**, *7* (35), 19546–19554.
- (29) Lee, M. W.; An, S.; Jo, H. S.; Yoon, S. S.; Yarin, A. L. Self-healing nanofiber-reinforced polymer composites. 2. Delamination/debonding and adhesive and cohesive properties. *ACS Appl. Mater. Interfaces* **2015**, *7* (35), 19555–19561.
- (30) Lee, M. W.; Sett, S.; Yoon, S. S.; Yarin, A. L. Fatigue of self-healing nanofiber-based composites: static test and subcritical crack propagation. *ACS Appl. Mater. Interfaces* **2016**, *8* (28), 18462–18470.
- (31) Lee, M. W.; Sett, S.; Yoon, S. S.; Yarin, A. L. Self-healing of nanofiber-based composites in the course of stretching. *Polymer* **2016**, *103*, 180–188.
- (32) Lee, M. W.; Yoon, S. S.; Yarin, A. L. Solution-blown core–shell self-healing nano-and microfibers. *ACS Appl. Mater. Interfaces* **2016**, *8* (7), 4955–4962.
- (33) Lee, M.; Yoon, S. S.; Yarin, A. L. Release of self-healing agents in a material: What happens next? *ACS Appl. Mater. Interfaces* **2017**, *9*, 17449–17455.
- (34) Stauffer, C. E. The measurement of surface tension by the pendant drop technique. *J. Phys. Chem.* **1965**, *69* (6), 1933–1938.
- (35) Hansen, F.; Rødsrud, G. Surface tension by pendant drop: I. A fast standard instrument using computer image analysis. *J. Colloid Interface Sci.* **1991**, *141* (1), 1–9.
- (36) Arashiro, E. Y.; Demarquette, N. R. Use of the pendant drop method to measure interfacial tension between molten polymers. *Mater. Res.* **1999**, *2* (1), 23–32.
- (37) Yarin, A. L. Drop impact dynamics: splashing, spreading, receding, bouncing... *Annu. Rev. Fluid Mech.* **2006**, *38*, 159–192.
- (38) Ringrose, P.; Bentley, M. *Upscaling Flow Properties*; Springer: Berlin, 2015; pp 115–149.
- (39) Sahu, R.; Sinha-Ray, S.; Yarin, A. L.; Pourdeyhimi, B. Drop impacts on electrospun nanofiber membranes. *Soft Matter* **2012**, *8*, 3957–3970.
- (40) Stachewicz, U.; Dijkstra, J. F.; Burdinski, D.; Yurteri, C. U.; Marijnissen, J. C. Relaxation times in single event electrospraying controlled by nozzle front surface modification. *Langmuir* **2009**, *25* (4), 2540–2549.
- (41) Luikov, A. V. Heat and mass transfer in capillary-porous bodies. *Adv. Heat Transfer* **1964**, *1*, 123–184.
- (42) Luikov, A. V. *Heat and Mass Transfer in Capillary-porous Bodies*; Pergamon Press, Oxford, 1966.
- (43) Lucas, R. Ueber das Zeitgesetz des Kapillaren Aufstiegs von Flüssigkeiten. *Colloid Polym. Sci.* **1918**, *23*, 15–22.
- (44) Washburn, E. W. The dynamics of capillary flow. *Phys. Rev.* **1921**, *17*, 273–283.
- (45) Levich, V. G. *Physicochemical Hydrodynamics*; Prentice Hall, Upper Saddle River, NJ, 1962.
- (46) Lembach, A.; Tan, H. B.; Roisman, I. V.; Gambaryan-Roisman, T.; Zhang, Y.; Tropea, C.; Yarin, A. L. Drop impact, spreading, splashing and penetration in electrospun nanofiber mats. *Langmuir* **2010**, *26* (12), 9516–9523.
- (47) McCabe, W. L.; Smith, J. C.; Harriot, P. *Unit Operations of Chemical Engineering*; McGraw-Hill: New York, 1993.
- (48) Tikhonov, A. N.; Samarskii, A. A. *Equations of Mathematical Physics*; Pergamon Press: Oxford, 1963.